Numerical Modeling of Heat and Mass Diffusion in Compressible Low Speed Flows

Yun-Ho Choi*

(*Received November 20, 1997*)

Numerical modeling of the heat transfer and molecular mixing in an electrical furnace designed for the spectroscopic study of hydrogen/alkali-metal-vapor mixtures is described. The gases enter the furnace through three concentric tubes, the inner two of which contain the test gases while the outer contains a guard gas to protect the windows. The inner tubes terminate prior to the measurement section to allow the gases to mix. Heating is accomplished through contact with the wall of the outer tube. An implicit time-marching procedure including a preconditioning method is used to compute the coupled gas flows. The results show that optimum flow speeds occur at a Reynolds number of order ten. Higher speeds do not allow adequate heating or mixing and can become unsteady, while lower speeds allow considerable back diffusion in the concentric tubes.

Key Words: Spectroscopy, Heat and Mass Diffusion, Low Speed Compressible Flow, Preconditioning Method, Flow Coupling

1. Introduction

The direct absorption of solar radiation in a flowing gas is of interest for various energy conversion applications including solar-pumped lasers and solar thermal propulsion (Mattick, 1980, Shoji, 1984).

Unfortunately, second law restrictions limit the maximum concentration ratio of solar energy to levels that are significantly below the intensities required for supporting a highly absorbing plasma in common gases making it difficult to couple the radiant energy into the fluid. Alkali metal vapors with their characteristically low ionization energies are known to be the reasonably efficient broad-band absorbers at visible wavelengths, and represent a possible exception to this. The absorption of concentrated solar radiation by alkali metal vapors has been studied theoretically (Rault, 1985, Mattick, 1978) and experimentally (Dunning and Palmer, 1981). It appears that volumetric absorption of solar radia-

tion in pure alkali metal vapors can produce mild plasmas with maximum temperature approaching 4000K, a temperature high enough to be attractive for many applications (Stwalley, 1980). Unfortunately, the use of pure alkali vapors in open cycles is not practical and even in closed systems it would be preferable to use the alkali vapors as a seedant in other, more manageable gases. A mixture of hydrogen with a low seedant concentration of alkali metals appears to be promising for solar propulsion and possibly for other applications as well.

An important step in assessing the capabilities of hydrogen/alkali metal seedant mixtures is a characterization of their spectroscopy and reliable estimates of their absorptivity. Alkali metals form numerous hydrides (M_xH_y) when mixed with hydrogen at elevated temperatures (Wu and Ihle, 1982, Larson, 1987), and these hydrides and their ions may be more effective in providing broad-band absorption over the solar spectrum than pure alkali metal vapors. For this purpose, a plasma spectroscopy cell (PSC) has been developed to provide hydrogen-alkali metal mixtures for optical diagnosis at various concentrations,

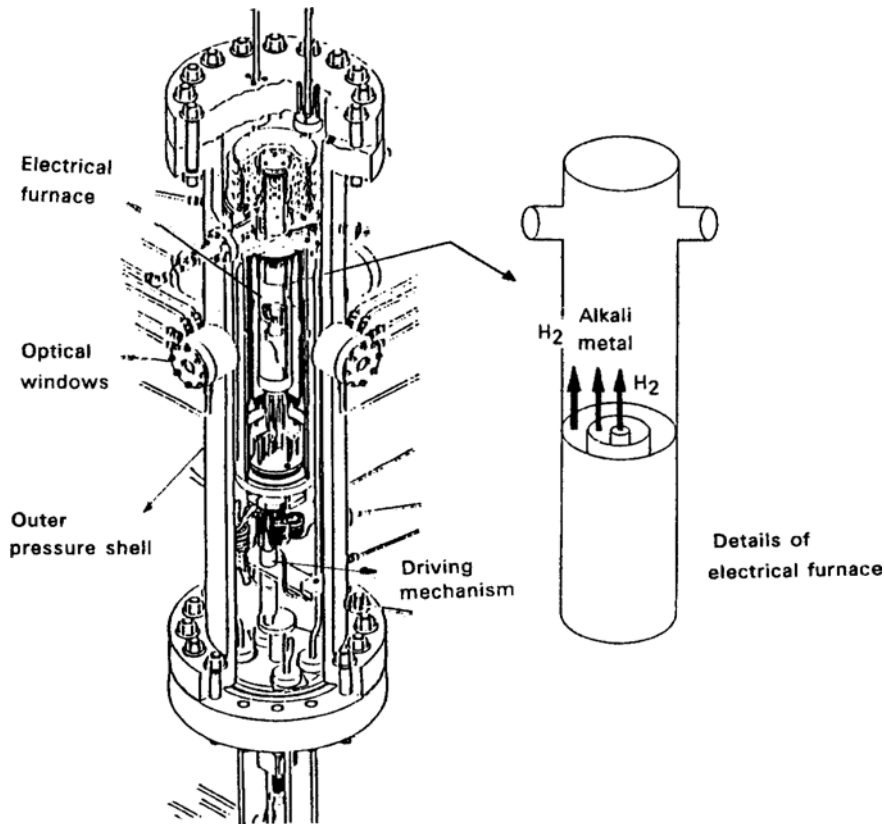* Department of Mechanical Engineering, Ajou University, Suwon 442-749, Korea

Fig. 1   A Cutaway view of plasma spectroscopy cell.

temperatures, and pressures. The PSC is a specially designed molybdenum-lined electrical furnace which contains a long axial tube through which hydrogen is heated as it flows upward through the furnace (see Fig. 1). Liquid metals are also supplied to the cell via a special evaporator that provides the desired concentrations of alkali–metal vapors. The mixing of the vapor and the hydrogen is accomplished by molecular processes after the vapor and hydrogen emerge from the co-annular tubes shown in Fig. 2. To provide for optical access, the cell contains four windows as shown in Fig. 1. When the gas reaches the window section, its characteristics can be documented by spectroscopy to determine the local temperature and the concentration of the gas mixture, and its absorptivity can be measured. The outermost of the three concentric tubes shown in Fig. 2 contains a guard gas used to protect these windows from damage.
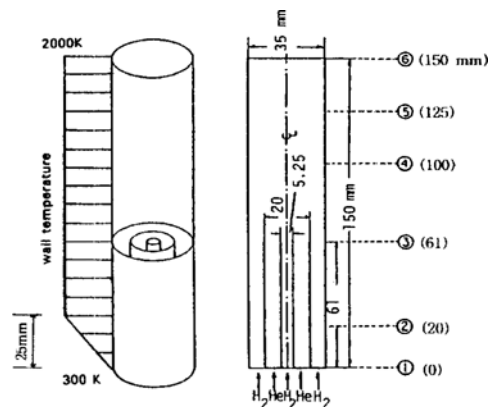

Fig. 2   Schematic of three concentric tubes arrangement and computational domain.

The numerous degrees of freedom in the experiment as well as the complexities in operating the PSC at elevated temperatures and pressures require a reasonably accurate understanding of the flow field to set initial flow rates and to aid in

understanding the measurements. Up to now, experimental or numerical studies for the PSC have not been reported and the present study is the first attempt to predict its performance. In the present study, development of a numerical model for computing the detailed characteristics of the mixing and heating in the cell is described. To gain initial understanding, an inert mixture of helium and hydrogen are used for this numerical study. Specific issues of interest include an assessment of maximum and minimum allowable flow rates and the corresponding heater size requirements. If gas velocities are set too high, the heat flux from the power supply will not be able to maintain the desired control over the gas temperature, and the intermolecular mixing will become too slow to provide the desired uniformity in the test section. High velocity flows may also give rise to vortex shedding and turbulence in the mixing layers which will further complicate the measurements. If the gas flow rate are too low, the guard gas will not function effectively.

2. Problem Formulation

The flowfield in the plasma spectroscopy cell is characterized by the low velocities and the low Reynolds numbers which ensure a thorough mixing of the hydrogen/alkali metal mixtures. In addition, hot walls are used to heat the flowing mixtures to elevated temperatures for diagnostic purposes, and the molecular weight differences render compressibility effects dominant in the flowfield. Consequently, we consider a numerical solution of the complete Navier–Stokes/mass-diffusion equations for a low Mach number, low Reynolds number compressible flow. It has been demonstrated that efficient numerical solution for these diffusion–controlled flows can be obtained by the use of preconditioning procedures (Turkel, 1987, Pletcher and Chen, 1993, van Leer et al, 1991, Choi and Merkle, 1993, Venkateswaran and Merkle, 1995). These preconditioning procedures were, however, developed for the standard Navier–Stokes equations and in the present study, the preconditioning procedure (Choi and Merkle, 1993, Venkateswaran and Merkle, 1995) is newly

extended to the viscous flows with mass diffusion to investigate the diffusion effects of species as well as heat and momentum.

The corresponding preconditioned Navier–Stokes/mass diffusion equations in generalized axisymmetric coordinates is :

$$
\Gamma \frac{\partial Q}{\partial t} + \frac{\partial E}{\partial \xi} + \frac{\partial F}{\partial \eta} = \frac{\partial}{\partial \xi}\Big[R_{\xi\xi}\frac{\partial}{\partial \xi}(JQ/y)
$$
$$
+ R_{\xi\eta}\frac{\partial}{\partial \eta}(JQ/y) \Big] + \frac{\partial}{\partial \eta}\Big[R_{\eta\xi}\frac{\partial}{\partial \xi}(JQ/y)
$$
$$
+ R_{\eta\eta}\frac{\partial}{\partial \eta}(JQ/y) \Big] + H
\qquad (1)
$$

where Q is the primary dependent vector, E and F are the inviscid flux vectors, H is a source vector that arises due to the axisymmetric geometry, and Γ is a preconditioning matrix that is defined upon the scaling eigenvalues of a system of the equations to the same order of magnitude. The matrices R are diffusion coefficient matrices that contain the viscosity μ, thermal conductivity k, and the binary diffusion coefficient D. The variables ξ and η are the transformed coordinate, and J is the Jacobian of the transformation. These vectors and matrices take the following form :

$$
Q = J^{-1}y[p,\ u,\ v,\ T,\ y_i]^T
$$
$$
E = J^{-1}y[\rho U,\ \rho uU + \xi_x p,\ \rho vU + \xi_y p,
$$
$$
(e + p) U,\ \rho U y_i]
\qquad (2)
$$
$$
F = J^{-1}y[\rho V,\ \rho uV + \eta_x p,\ \rho vV + \eta_x p,
$$
$$
(e + p) V,\ \rho V y_i]
$$
$$
H = J^{-1}[0,\ h_2,\ h_3,\ 0,\ 0]
$$

where,

$$
h_2 = -\frac{2}{3}\left(\xi_x\frac{\partial \mu v}{\partial \xi} + \eta_x\frac{\partial \mu v}{\partial \eta} \right)
$$
$$
h_3 = p - \frac{4}{3}\cdot\frac{\mu v}{y} + \frac{2}{3}\mu\left(\xi_x\frac{\partial u}{\partial \xi} + \eta_x\frac{\partial u}{\partial \eta} \right) - \frac{2}{3}
$$
$$
v\left(\xi_y\frac{\partial \mu}{\partial \xi} + \eta_y\frac{\partial \mu}{\partial \eta} \right) - \frac{2}{3}\left(\xi_x\frac{\partial \mu u v}{\partial \xi} + \eta_x\frac{\partial \mu u v}{\partial \eta} \right)
$$
$$
+ \xi_y\frac{\partial \mu v^2}{\partial \xi} + \eta_y\frac{\partial \mu v^2}{\partial \eta} \right)
\qquad (3)
$$

The preconditioning matrix Γ is chosen to maintain well-conditioned eigenvalues in the inviscid flux vectors when the diffusion terms are small (Re larger than about 100), and to provide proper scaling of the viscous terms when the viscous terms are dominant (Re less than 100). Its

form is given by

$$
\Gamma =
\begin{bmatrix}
-\dfrac{1}{u^2+v^2} & 0 & 0 & 0 & 0 \\[2mm]
-\dfrac{u}{u^2+v^2} & \rho & 0 & 0 & 0 \\[2mm]
-\dfrac{v}{u^2+v^2} & 0 & \rho & 0 & 0 \\[2mm]
\dfrac{e+p}{\rho(u^2+v^2)}-1 & \rho u & \rho v & \dfrac{\gamma\rho R}{\gamma-1} & 0 \\[2mm]
-\dfrac{y_i}{u^2+v^2} & 0 & 0 & 0 & \rho
\end{bmatrix}
\qquad (4)
$$

The matrices R depend on the matrices of the transformation and four sparse matrices R_{xx}, R_{xy}, R_{yx}, R_{yy}.

$$
\begin{aligned}
R_{\xi\xi} &= J^{-1}(\xi_x^2 R_{xx}+\xi_x\xi_y R_{xy}+\xi_x\xi_y R_{yx}+\xi_y^2 R_{yy}) \\
R_{\xi\eta} &= J^{-1}(\xi_x\eta_x R_{xx}+\xi_x\eta_y R_{xy} \\
&\quad +\xi_y\eta_x R_{yx}+\xi_y\eta_y R_{yy}) \\
R_{\eta\xi} &= J^{-1}(\xi_x\eta_x R_{xx}+\eta_x\xi_y R_{xy} \\
&\quad +\eta_y\xi_x R_{yx}+\xi_y\eta_y R_{yy}) \\
R_{\eta\eta} &= J^{-1}(\eta_x^2 R_{xx}+\eta_x\eta_y R_{xy}+\eta_x\eta_y R_{yx}+\eta_y^2 R_{yy})
\end{aligned}
\qquad (5)
$$

The sparse matrices R_{xx}, R_{xy}, R_{yx}, R_{yy} are :

$$
R_{xx}=\mathrm{Diag}\left(0,\ \frac{4}{3}\mu y,\ \mu y,\ \frac{ky}{C_p},\ \rho Dy\right)
$$

$R_{xy}=$ null matrix

$$
\text{with non-zero elements}
\begin{cases}
(2,\ 3)=-\dfrac{2}{3}\mu y \\[2mm]
(3,\ 2)=\mu y
\end{cases}
$$

$$
R_{yx}=R_{xy}^T
$$

$$
R_{yy}=\mathrm{Diag}\left(0,\ \mu y,\ \frac{4}{3}\mu y,\ \frac{ky}{C_p},\ \rho Dy\right)
$$

In these expressions, x and y represent the axial and radial coordinates in the physical coordinate system. The variable p denotes pressure; u, v, and T are the velocity components and the temperature. The y_i represents the mass fractions of the various species. The quantities U and V are the contravariant velocities. The properties, μ, k and D are taken as a power law function of the temperature as follows (White, 1974).

$$
\mu = \mu_{\mathrm{ref}}\left(\frac{T}{T_{\mathrm{ref}}}\right)^{0.75}
$$

$$
k = k_{\mathrm{ref}}\left(\frac{T}{T_{\mathrm{ref}}}\right)^{0.75}
\qquad (7)
$$

$$
D = D_{\mathrm{ref}}\left(\frac{T}{T_{\mathrm{ref}}}\right)^{0.75}
$$

In the present study, Dufour effects: energy flux

due to the mass diffusion processes are ignored in the energy equation, as is customary in combustion problems. In addition, we treat only chemically inert flows so the species equations include only mass diffusion and convection.

The addition of species equations to the preconditioned Navier–Stokes equations does not alter the characteristics of the original system of equations and it remains well conditioned. The eigenvalues of the system of equations are

$$
\left(U,\ U,\ \frac{U(1+M^2)+c'}{2},\ \frac{U(1+M^2)-c'}{2},\ U\right)
\qquad (8)
$$

Here, the pseudo-acoustic speed c' is defined by,

$$
c'^2 = U^2(1-M^2)^2+4(u^2+v^2)(\xi_x^2+\xi_y^2)
\qquad (9)
$$

The pseudo-acoustic speed c' is the same order as the particle velocity u, and this ensures that three eigenvalues are always positive, while one is negative for subsonic flow. The preconditioned equations given in Eq. (1) has been shown to give convergence rates that are independent of Mach number and Reynolds number (Choi and Merkle, 1993, Venkateswaran and Merkle, 1995).

3. Numerical Solution Procedure

The numerical solution of Eq. (1) is obtained by using an Euler implicit discretization in time along with central differencing in space for both the inviscid and the viscous terms. Efficient solution of the resulting matrix requires that an approximate factorization such as the Douglas–Gunn procedure (1964) be used. All equations are solved simultaneously at each time step, with the solution of a block tridiagonal sweep being required for each coordinate direction. In a discrete form Eq. (1) becomes :

$$
\left[I+\Delta t P^{-1}\left(\frac{\partial}{\partial\xi}A-\frac{\partial}{\partial\xi}R_{\xi\xi}\frac{\partial}{\partial\xi}\frac{J}{y}\right)\right]
$$
$$
\left[I+\Delta t P^{-1}\left(\frac{\partial}{\partial\eta}B-\frac{\partial}{\partial\eta}R_{\eta\eta}\frac{\partial}{\partial\eta}\frac{J}{y}\right)\right]\Delta Q
$$
$$
= -\Delta t P^{-1}R
\qquad (10)
$$

where R is the residual of the steady state version of Eq. (1).

$$R = \frac{\partial}{\in \xi}\left(E - R_{\xi\xi}\frac{\partial(JQ)}{\partial\xi} - R_{\xi\eta}\frac{\partial(JQ)}{\partial\eta}\right) \quad (11)$$
$$+ \frac{\partial}{\partial\eta}\left(F - R_{\eta\xi}\frac{\partial(JQ)}{\partial\xi} - R_{\eta\eta}\frac{\partial(JQ)}{\partial\eta}\right) + H$$

Here A, B, and D are the Jacobians of the vectors E, F and H, and the matrix, P, is defined as $P = \Gamma - \Delta t D$. This formulation differs from an approximately factored traditional algorithm only in the calculation of the preconditioning matrix, and hence additional computational cost is negligible.

4. Boundary Conditions

The flow domain of interest is shown on Fig. 2. In the present study, considering that the flowfield is axisymmetric, we compute only half of this domain. Boundary conditions are specified at the upstream and downstream ends and on all side walls. At the upstream boundary, velocity (u), temperature (T) and concentration profiles (y_i) are specified. On all walls, a no-slip condition ($u = v = 0$) is enforced. On the outer wall, these are augmented by a specified wall temperature distribution as shown in Fig. 2, while the inner walls are assumed to be thin and highly conducting in the radial direction. (For the cases reported herein, Biot number ranges from 2×10^{-5} to 5×10^{-4} and this small Biot number indicates the internal conduction resistance is negligibly small.) Thermal boundary conditions on the inner walls are that the heat flux is continuous and the fluid temperatures on the two sides of the wall are equal ($T_1 = T_u$, $\left.\frac{\partial T}{\partial\eta}\right|_l = \left.\frac{\partial T}{\partial\eta}\right|_u$, where l and u denote the lower and upper sides of the wall). These velocity and temperature boundary conditions are complemented by a requirement for zero mass diffusion to the wall $\left(\frac{\partial y_i}{\partial\eta} = 0\right)$ and by enforcing the zero normal pressure gradient $\left(\frac{\partial p}{\partial\eta} = 0\right)$. These latter two conditions are applied on all walls.

The boundary conditions at the upstream and downstream ends are as follows. At the upstream boundary, the inlet velocity, stagnation temperature and the species concentration of the incoming stream are specified for all three tubes. For the cases reported here, the fully developed velocity

profiles with uniform temperature are used throughout. These four boundary conditions are supplemented by an application of the axial momentum equation on the upstream boundary. This axial momentum equation determines the streamwise pressure gradient at the upstream end.

At the downstream boundary, the static pressure is fixed. To reflect the dominance of the viscous terms, we also specify the following conditions,

$$u_{\xi\xi} = v_{\xi\xi} = T_{\xi\xi} = y_{i\xi\xi} = 0 \quad (12)$$

Symmetry conditions were imposed implicitly at the centerline.

5. Flow Coupling Inside the Tubes

Although the fluid is in three separate tubes at the upstream end of the computational domain, the flow in this region is still coupled. One coupling arises at the exit plane where pressure feedback from the downstream mixing region couples the pressures in the three tubes. At the exit of internal tubes, a condition which ensures the continuity of the pressure on either side of the wall $\left(p_l = p_u, \left.\frac{\partial p}{\partial\eta}\right|_l = -\left.\frac{\partial p}{\partial\eta}\right|_u\right)$ is imposed and this pressure balance determines distinct pressure gradients and upstream pressure levels in each of the three tubes.

A second coupling, and one that is more numerically significant, is the continuity of heat flux and temperature at the internal walls. This coupling causes the ξ and η sweep operators (Eq. (10)) to lose their tridiagonal characters. To circumvent this difficulty, we have used non-sequential grid numbering as shown in Fig. 3. The grid lines on the outer surface of the two inner walls are numbered out of sequence. This causes no difficulty in the ξ-sweep, but gives non-tridiagonal operators shown in Fig. 4, while the fluid is inside or outside of the tubes.

The partitioning used to solve these matrices is also shown in Fig. 4. In the multiple-tube region, this partitioning leads to the tridiagonal matrix, T_1, the diagonal matrix A_3 and the sparse rectangular matrices A_1 and A_2. With this partitioning, the equations can be written as,
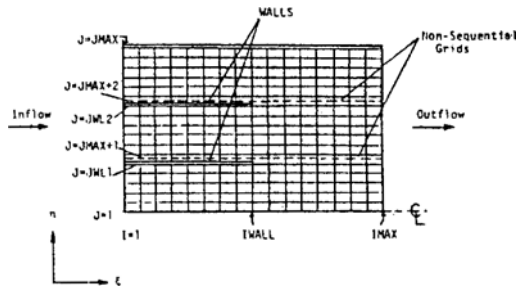
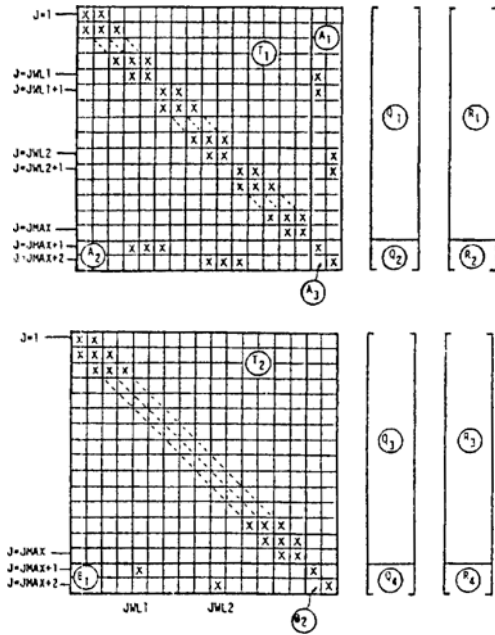**Fig. 3** Details of grid numbering procedures.

Fig. 4 Partitioning procedure. a) Matrix structure for η-sweep operator for region inside the concentric tubes $(1 < \text{IWALL})$ b) Matrix structure for η-sweep operator in downstream mixing region. $(1 > \text{IWALL} + 1)$.

$$T_1 Q_1 + A_1 Q_2 = R_1$$
$$A_2 Q_1 + A_3 Q_2 = R_2 \qquad (13)$$

The solution vectors, Q, are then easily obtained as,

$$Q_1 = [T_1 - A_1 A_3^{-1} A_2]^{-1} [R_1 - A_1 A_3^{-1} R_2]$$
$$Q_2 = A_3^{-1} [R_2 - A_2 Q_1] \qquad (14)$$

The matrix $T_1 - A_1 A_3^{-1} A_2$ is not tridiagonal but can be made so by a single step of a standard Gaussian elimination procedure making the solution of this matrix nearly competitive with a

tridiagonal matrix.

In the downstream mixing region, the solution vector Q is obtained by the partitioning shown on Fig. 4 :

$$T_2 Q_3 = R_3$$
$$B_2 Q_4 = R_4 - B_1 Q_3 \qquad (15)$$

Here. T_2 is a tridiagonal matrix and, hence, additional effort which uses Gaussian elimination is not necessary.

6. Results and Discussioneke

To understand the nature of the diffusion of heat and mass in the plasma spectroscopy cell, both cold flow and hot flow calculations have been made for a range of Reynolds numbers (Re $= 2 \sim 2000$). The corresponding Mach number varies from 5.7×10^{-6} to 5.7×10^{-3}. A schematic of the computational domain is shown in Fig. 2. All calculations were performed on a 60×61 meshes. This relatively small grid is chosen because the present study represents diffusion -dominated flows which include smooth property variations in the most part of flow regions. A further study with a larger grid size (60×81) shows that the solution accuracy is similar as that of 60×61 case.

Results for a cold flow of hydrogen and helium through the PSC are given in Fig. 5 for four Reynolds number conditions ranging from 2 up through 2000.Figure 5 shows velocity, concentration and pressure contours at each of the Reynolds number conditions. For all cases, the inlet velocity profile in each tube was taken as fully developed (parabolic profile) and the same average velocity was used for each tube. The variation in Reynolds number was accomplished by changing the average velocity at the inlet. Reynolds number values are based on the average inlet velocity, the diameter of the large tube and the viscosity of hydrogen at the inlet temperature. In all calculations, Prandtl and Schmidt numbers were 0.7.

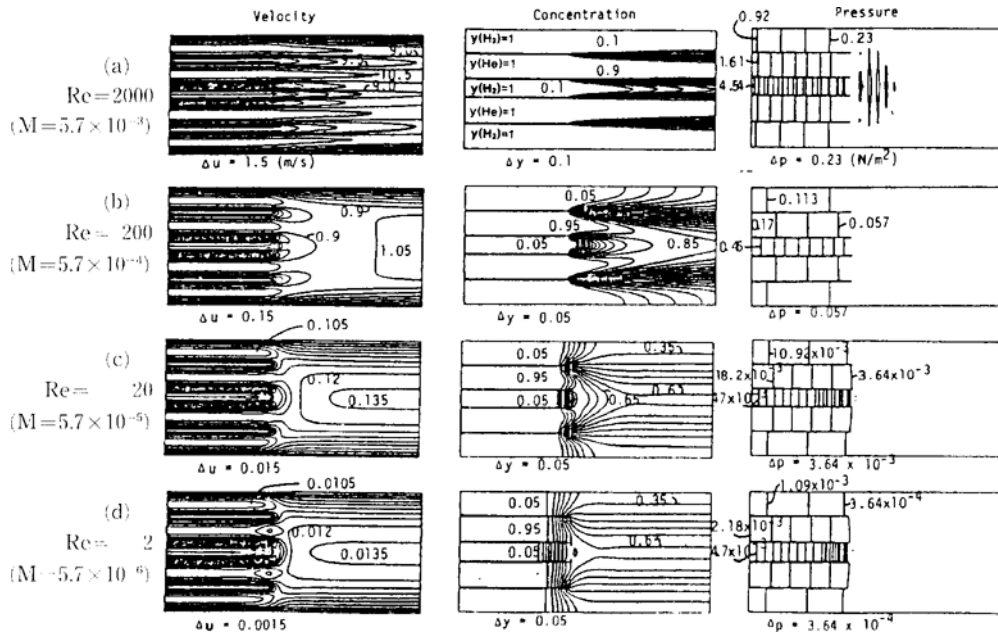At the highest Reynolds number of 2000, the effects of both viscous and mass diffusion are

Fig. 5 Velocity, concentration and pressure distributions for Reynolds numbers of 2, 20, 200 and 2000 at cold wall conditions, Tw = 300K. (The concentration contours shown are for helium).

quite small. The velocity contours inside the concentric tubes show parallel lines which indicate fully developed flow and the concentration profiles show a slow rate of diffusion after the individual species emerge from the separate tubes. The pressure gradient contours show nearly linear gradients in each tube, although the magnitude of dp/dx is considerably different in the three tubes because of differences in the individual tube Reynolds numbers.

Convergence characteristics for the present computation are shown in Fig. 6.This convergence rate is representative of the other Reynolds number cases as well. It takes about 3000 iterations to reduce L_2 norm of $\Delta Q/Q$ by six order of magnitude. Compared with the convergence of the standard time-marching method which will be extremely slow at these very incompressible flow speeds, it is clear that the present approach enables convergence with efficiencies that are equal to those normally observed in high subsonic flows.

At the a Reynolds number of 200, the rate of molecular mixing is dramatically higher although the gas constituents are still considerably non
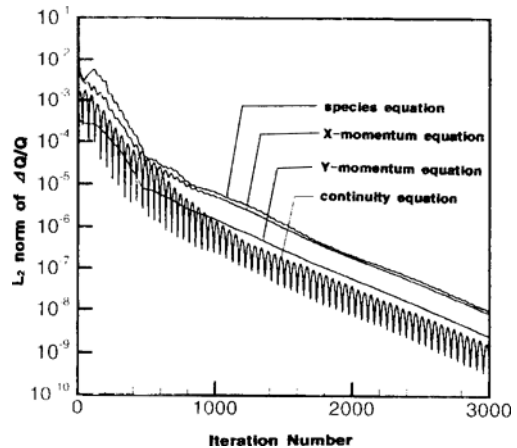

Fig. 6 Convergence characteristics for computations of flow inside the plasma spectroscopy cell at Re = 2000. Cold flow case.

-uniform at the exit plane. The velocity contours in the mixing zone still show a boundary layer growth along the walls, but the wakes of the individual tubes diffuse much more rapidly than for the Re=2000 case.

The calculations for the Reynolds number of 20 show fully developed velocity profiles at the downstream end, thus suggesting that this

Reynolds number is reasonable for testing. Conditions at Reynolds number of 2 rapidly lead to a well-characterized fully developed velocity profile. At this low Reynolds number we also observe a substantial amount of back diffusion inside the three small stream tubes so that the concentration profiles are nearly uniformly mixed by the exit. Such back diffusion could cause problems in the experiment and should be avoided.

Some representative axial velocity profiles for these cold wall cases are shown in Fig. 7.For the four Reynolds number cases, velocity profiles are presented at the six axial locations noted in Fig. 2. Note profiles 1, 2 and 3 are inside the concentric tubes whereas profiles 4, 5 and 6 are in the common mixing region. These axial velocity profiles, again, demonstrate the relatively slow rate of adjustment in the mixing region at Re = 2000 and the increasingly rapid approach to a fully developed flow at the lower Reynolds number. By contrast, the flow inside the individual tubes remains fully developed at the higher Reynolds numbers, but changes with distance at the lower Reynolds numbers. This variation with distance arises because of the back diffusion in

the tubes at low Reynolds numbers and its effect on properties inside the tube.

A similar set of calculations is shown in Fig. 8 for the case where the outer wall is heated to a temperature of 2000K according to the distribution given in Fig. 2.For these heated cases, the fluid properties(viscosity, thermal conductivity,
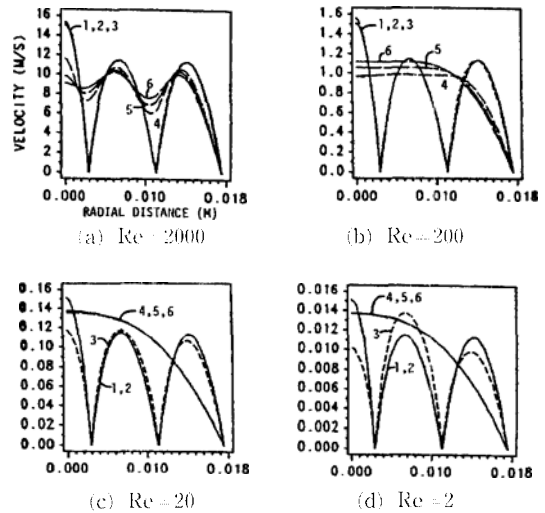

Fig. 7 Velocity profiles for various axial locations and various flow Reynolds numbers. Cold flow case
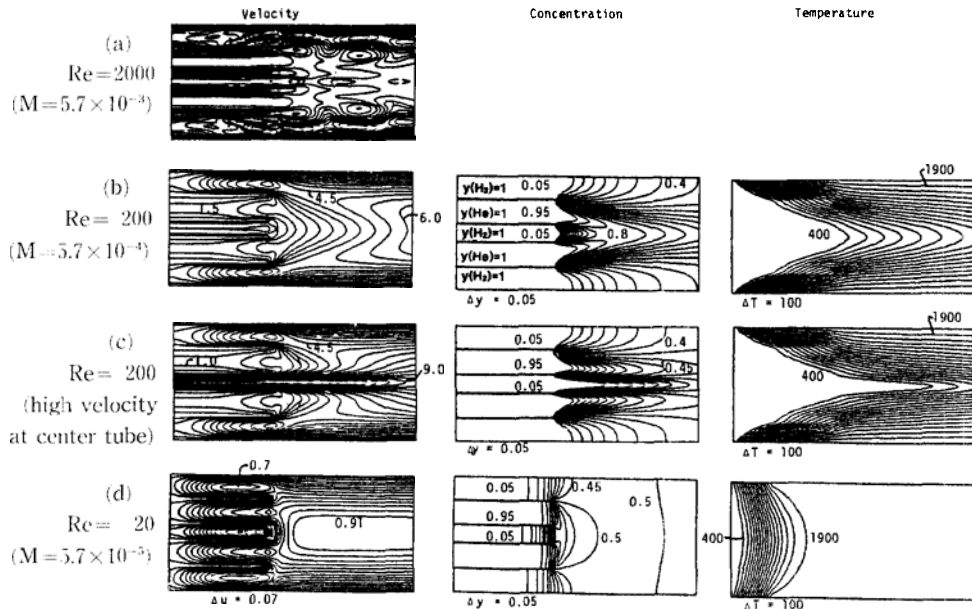

Fig. 8 Velocity, concentration and temperature contours for heated wall case (Tw = 2000K) at several flow conditions.(The concentration contours shown are for helium).

and mass diffusivity) are evaluated using the power law mentioned earlier.

At the Reynolds number of 2000, a steady state calculation is refused for convegence and when the unconverged results are plotted, a series of large eddies is present as indicated in Fig. 8(a). Because the current time-marching procedure is not physical, these cannot be interpreted as a time-accurate unsteady result, but the organized nature of the flow and the inability to converge suggests that a steady solution may not exist and that unsteady vortex shedding may be present. Further studies, however, might be necessary to ensure the current flow behavior.

This convergence difficulty is readily seen to be a function of Reynolds number because at a Reynolds number of 200, convergence is attained easily at a rate similar to that observed for cold flow. These results are shown on Fig. 8(b). Because the pressure contours in the presence of heating are similar to those for cold flow, we here show the temperature contours (along with velocity and concentration contours) in place of the pressure contours. Comparison of the cold flow results at Re=200 with the present ones shows that the increased wall temperature has little effect on the concentration profiles, even though the

velocity profiles are considerably different. The presence of heat diffusion causes the velocity profile to continue to change with distance as compared with the approach to a fully developed flow observed in the cold flow case. In particular, the heat diffusion causes the flow to continue to accelerate.

The Re=200 results in Fig. 8(b) are for the same average velocity in all three tubes. To find the effect of unequal velocities in the tubes, the gas in the center tube is increased by a factor of ten in Fig. 8(c), while the velocities in the other two tubes remain the same as in Fig. 8(b). The higher velocity of the gas in the central tube decreases both heat and mass transfer in the central tube, so the inner stream remains relatively cold and unmixed. It is also interesting to note that the inner tube velocity in Fig. 8(c) is the same as that in Fig. 8(a), but there is no indication of instability here as shown in Fig. 8(a).

At a Reynolds number of 20 (Fig. 8(d)) both heat and mass diffuse rapidly into the center of the tube as noted in the cold flow case in Fig. 5. At this low speed, the diffusion of heat is so fast that a fully developed flow is set up in the common passage nearly as rapidly as it was without heat addition. The resulting temperature increase
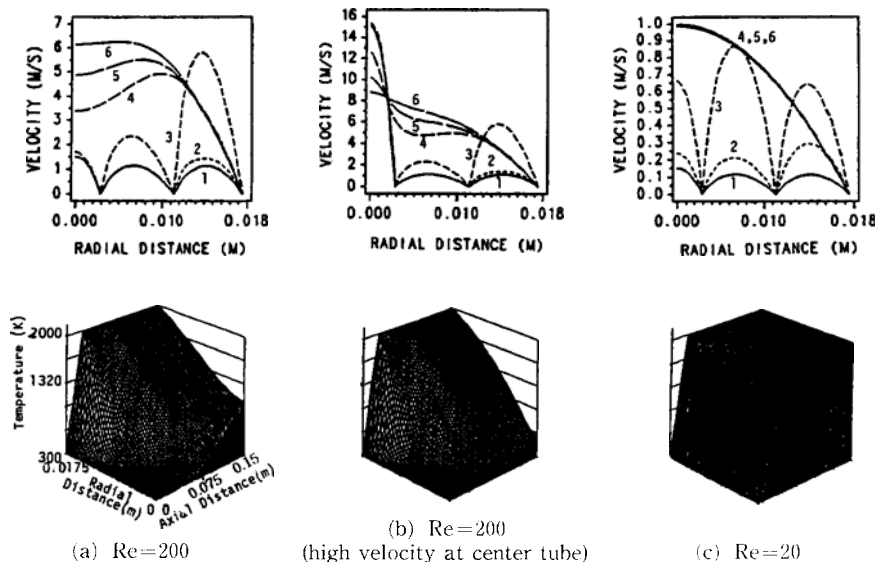

(a) Re=200   (b) Re=200 (high velocity at center tube)   (c) Re=20

Fig. 9   Velocity profiles and temperature contour surfaces for heated wall case, Tw=2000K. Identification numbers refer to axial locations in Fig. 2.
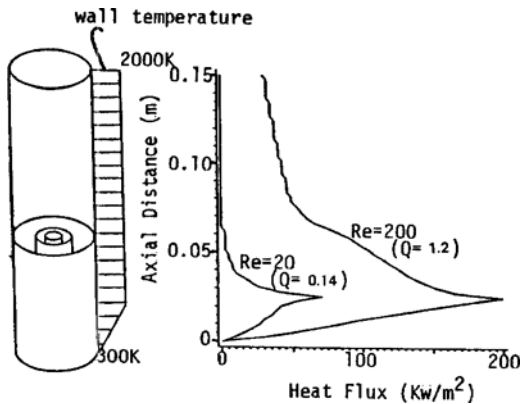
wall temperature

Fig. 10 Heat flux to the walls for 2000K wall temperature. Re=200 and 20.

does, however, result in a higher velocity in the fully developed region. Again, back-diffusion of mass is seen in the tubes, and the temperature profiles rapidly equilibrate to the wall temperature. The Reynolds number 20 case again suggests uniform mixedness in the test section. Additional analyses of methods for maximizing window protection by controlling the outer stream remain to be done, but this appears to be a reasonable Reynolds number at which to attempt control.

The corresponding axial velocity profiles for this case are shown in Fig. 9 along with three -dimensional plots of the gas temperature. The heat addition causes the velocity profiles to accelerate strongly in comparison to the cold wall case (Fig. 7). At the Reynolds number of 200, the flow along the outer wall accelerates first followed by that in the inner two tubes. The continued heat diffusion in the downstream mixing region causes the velocity on the centerline to continue to accelerate until the downstream end is reached. The temperature contour plot shows the center-line temperature is almost unaffected until $x = 0.06$ (m) after which it increases almost linearly. At this Reynolds number, the temperature in the core of the cell is still considerably lower than that at the walls, indicating that this velocity is too fast for experimental study since the central temperature is only about half the wall temperature.

When the central tube velocity is increased by 10 (Fig. 9(b)), the velocity on the centerline is seen to decrease with distance as the slower outer

streams slow it down. For this case, the central stream is heated to only about 20% of the wall temperature before it reaches the downstream boundary.

The Re=20 case in Fig. 9(c) shows that fully developed velocity profiles are reached very quickly after the gases enter the mixing region. The temperature contour shows this is because the gas in the center tube has reached the wall temperature before it exits the tube. This case represents an efficient heating condition, although a method for ensuring window protection must still be investigated.

An important parameter for the design of the plasma cell is the required heat flux to the wall to maintain the indicated wall temperatures. Figure 10 shows the axial distribution of the heat flux for the Re=200 and Re=20 cases. Peak heating rates occur near the end of the wall temperature gradient and reach levels of about 200 and 65 Kw/m^2, respectively, for these two flow rates. The total integrated heat flux into the gases in these two cases is 1.2 Kw at Re=200 and 0.14 Kw at Re= 20.

7. Summary

An implicit time-marching procedure using a preconditioning method has been developed and applied to the design of a plasma spectroscopy cell for measuring optical properties of gas mixtures at elevated temperatures and pressures. This preconditioning procedure ensures rapid convergence at the low speed and viscous condition.

The flowfield in the PSC is composed of an initial heating region where individual gas streams flow in three concentric tubes. Prior to the test section, these individual streams merge into a common chamber where they mix by diffusion. Important aspects of the experiment are ensuring that the inner gas flow gets heated amply and that it is well-mixed with the middle stream while the outer stream remains relatively unmixed to protect the windows. The flows in the three tubes are coupled by heat flux and temperature continuity across the inner walls and a common pressure at the tube exit.

Computations of the flow for cold wall conditions give an indication of the diffusion rates to be encountered and the appropriate Reynolds number regimes. These are contrasted to the cases with heated walls (Tw=2000K). At a Reynolds number of 2000, the addition of heat apparently makes a previously stable flowfield unstable so that large scale vortices appear, but the gas flow velocities are also too high to allow sufficient heating of the gas. At a Reynolds number of 200, the flowfield appears steady, but the central portion of the flow still does not approach to the temperature of hot walls. Calculation at a Reynolds number of 20 suggests this is about an optimum condition. At this condition, the central portion of the gas essentially reaches the wall temperature and back diffusion inside the tubes is still relatively minor. Some optimization of the outer stream may be required to optimize window protection. Lower Reynolds number conditions appear to allow too much back diffusion.

References

Choi, Y. H. and Merkle, C. L., 1993, "The Application of Preconditioning in Viscous Flows," *Journal of Computational Physics*, Vol. 105, pp. 207~223.

Douglas, J. and Gunn, J. E., 1964, "A General Formulation of Alternating Direction Method -Part I. Parabolic and Hyperbolic Problem," *Numerishe Mathematik*, Vol. 82, pp. 428~453.

Dunning, G. J. and Palmer, A. J., 1981, "Towards a High-Temperature Solar Electric Converter," *J. Appl. Phys.*, Vol. 52, pp. 7086 ~7091.

Larson, C. W., 1987, "Kinetics, Thermodynamics, and Spectroscopy of Mixtures of Hydrogen and Alkali Metal Vapors at Temperatures and Pressures Approaching 3000K and 100 Atmospheres," *Joint Meeting of the Western States and Japanese Sections of the Combustion Institute*, Honolulu, HA, NOV. 22~25.

Mattick, A. T., 1980, "Coaxial Radiative and Convective Heat Transfer in Gray and Nongray Gases," *J. Quant. Spectrosc. Radiat. Transfer*, Vol. 24, pp. 323~334.

Mattick, A. T., 1978, "Absorption of Solar Radiation by Alkali Vapors," *Radiation Energy Conversion in Space, Progress in Astronautics and Aeronautics*, Vol. 61, pp. 159~171.

Pletcher, R. H. and Chen, K. H., 1993, "On Solving the Compressible Navier-Stokes Equations for Unsteady Flows at Very Low Mach Numbers," AIAA-93-3368-CP, pp. 765~775.

Rault, D. F. G., 1985, "Radiation Energy Receiver for Solar Propulsion System," *J. Spacecraft and Rockets*, Vol. 22, pp. 642~648.

Shoji, J. M., 1984, "Potential of Advanced Solar Thermal Propulsion," Orbit-Raising and Maneuvering Propulsion: Research Status and Needs, Progress in Astronautics and Aeronautics, Vol. 89, pp. 30~47.

Stwalley, W. C., 1980, "Alkali Metal Vapors: Laser Spectroscopy and Applications," *Optical Engineering*, Vol. 19, pp. 71~84

Turkel, E., 1987, "Preconditioned Methods for Solving the Incompressible and Low Speed Compressible Equations," *Journal of Computational Physics*, Vol. 72, pp. 277~298.

van Leer, B., Lee, W. T. and Roe, P. L., 1991, "Characteristic Time-Stepping or Local Preconditioning of the Euler Equations," in *AIAA 10th Computational Fluid Dynamics Conference*.

Venkateswaran, S. and Merkle, C. L., 1995, "Analysis of Time-Derivative Preconditioning for the Navier-Stokes Equations," in 6th *International Symposium on Computational Fluid Dynamics*.

White, F. M., 1974, *Viscous Fluid Flow*, McGraw Hill.

Wu, C. H. and Ihle, H. R., 1982, "Thermochemistry of the Dimer Lithium Hydride Molecule," *Metal Bonding and Interactions in High Temperature Systems*, J. L. Gole and W. C. Stwalley, Editors, (ACS Symposium Series)